Accepted Manuscript

Dual-Color Photoacoustic Lymph Node Imaging Using Nanoformulated Naphthalocyanines

Changho Lee, Jeesu Kim, Yumiao Zhang, Mansik Jeon, Chengbo Liu, Liang Song, Jonathan F. Lovell, Chulhong Kim

Please cite this article as: Lee C, Kim J, Zhang Y, Jeon M, Liu C, Song L, Lovell JF, Kim C, Dual-Color Photoacoustic Lymph Node Imaging Using Nanoformulated Naphthalocyanines, *Biomaterials* (2015), doi: 10.1016/j.biomaterials.2015.09.023.

This is a PDF file of an unedited manuscript that has been accepted for publication. As a service to our customers we are providing this early version of the manuscript. The manuscript will undergo copyediting, typesetting, and review of the resulting proof before it is published in its final form. Please note that during the production process errors may be discovered which could affect the content, and all legal disclaimers that apply to the journal pertain.

Dual-Color Photoacoustic Lymph Node Imaging Using Nanoformulated Naphthalocyanines

Changho Lee[1,§], Jeesu Kim[1,§], Yumiao Zhang[2], Mansik Jeon[1,4], Chengbo Liu[3], Liang Song[3], Jonathan F. Lovell[2,*], and Chulhong Kim[1,*]

[1]*Future IT Innovation Laboratory, Department of Creative IT Engineering and Electrical Engineering, Pohang University of Science and Technology (POSTECH), 77 Cheongam-ro, Nam-gu, Pohang, Gyeongbuk, Republic of Korea*

[2]*Department of Biomedical Engineering, University at Buffalo, The State University of New York, Buffalo, NY 14260, USA*

[3]*Institute of Biomedical and Health Engineering, Shenzhen Institutes of Advanced Technology, Chinese Academy of Sciences, 1068 Xueyuan Boulevard, Shenzhen 518055, China*

[4]School of Electronics Engineering, College of IT Engineering, Kyungpook National University, 80 Daehak-ro, Bukgu, Daegu. 702101, Korea

[§]*These authors contributed equally on this work.*
[*]*Corresponding authors: chulhong@postech.edu and jflovell@buffalo.edu*

Keywords: Photoacoustic imaging, Optoacoustic, Organic nanoparticles, Naphthalocyanines, Sentinel lymph node mapping.

Abstract

Demarking lymph node networks is important for cancer staging in clinical practice. Here, we demonstrate *in vivo* dual-color photoacoustic lymphangiography using all-organic nanoformulated naphthalocyanines (referred to as nanonaps). Nanonap frozen micelles were self-assembled from two different naphthalocyanine dyes with near-infrared absorption at 707 nm or 860 nm. These allowed for noninvasive, nonionizing, high resolution photoacoustic identification of separate lymphatic drainage systems *in vivo*. With both types of nanonaps, rat lymph nodes buried deeply below an exogenously-placed 10 mm thick layer of chicken breast were clearly visualized *in vivo*. These results show the potential of multispectral photoacoustic imaging with nanonaps for detailed mapping of lymphatic drainage systems.

1. Introduction

The sentinel lymph node biopsy (SLNB) has become a standard clinical procedure as a less invasive preference to axillary lymph node dissection in breast cancer patients. In clinical practice, prior to SLNB, sentinel lymph nodes (SLNs) are identified intraoperatively to guide the surgical operations [1-3]. The typical clinical protocol includes: (1) injection of radioactive colloids (e.g., ^{99m}Tc), (2) rough identification of the SLN's position using a Geiger counter, (3) injection of a colored dye (e.g., methylene blue), (4) exposure of the SLN via visual identification, and (5) surgical removal of the SLN for histology [4, 5]. From a safety point of view, conventional SLNBs use ionizing radiation and are not completely free from morbidity; associated complications such as seroma, lymphedema, nerve injury, and limitation of motion often occur [6, 7]. More problematically, the low spatial resolution of the Geiger counter makes it impossible to noninvasively pinpoint the exact position of the SLN [8]. Therefore, noninvasive, nonionizing, and accurate imaging of SLNs is critical to relieve the burden of the cancer patients by providing possibilities to perform minimally invasive image-guided axillary staging using fine needles or noninvasively identify the metastatic SLNs using molecular targeting agents [9].

Recently, photoacoustic imaging (PAI) has been explored as a noninvasive lymph node mapping tool in both small animals and human breast cancer patients because it can sensitively visualize contrast enhanced SLNs in deep tissues (i.e., up to ~ 50 mm) with good ultrasonic spatial resolution (i.e., ~ 0.5 mm) [10-13]. Organic dyes such as methylene blue and indocyanine green have been typically used as PA lymph node tracers. However, these small molecules have concentration-dependent spectral properties and flow too quickly into successive lymph nodes from the sentinel node resulting in a high rate of false positives in axillary staging [14-16]. In

addition, other inorganic contrast agents such as gold- and carbon-based nanostructures have been widely exploited as PA lymph node agents in small animals due to strong localized surface plasmon resonance, biocompatibility, and efficient molecular targeting capability [17-21]. However, inorganic materials generally are associated with long-term safety concerns. Multispectral family of nanoparticles have been demonstrated with this approach, but not in the context of lymphatic mapping [22].

Conventional medical imaging tools typically use monochromatic energy sources. Thus, one contrast agent can be visualized at a single acquisition, and the acquired data is limited to a single spectrum. Optical imaging is uniquely able to provide multi-spectral parameters of multicolor contrast agents [23-26]. However, conventional planar fluorescence imaging or high resolution fluorescence microscopy suffers from either poor spatial resolution in deep tissues or shallow penetration, respectively.

In this study, we have used organic nanoformulated naphthalocyanines (referred to as nanonaps) for dual-color PA SLN mapping *in vivo*. The discovery of nanonaps was recently reported [27] and unique features include (1) exceptionally strong near-infrared (NIR) absorption in solution of greater than 1000 (additionally, these are nearly 100 times more absorbing than gold nanorods at the same mass concentration), (2) no potential heavy metal toxicity due to its organic nature, (3) multi-color imaging capability due to wide spectral tuning range in the NIR region, and (4) non-shifting spectral stability at ultrahigh optical densities. Nanonaps are formed from kinetically frozen Pluronic triblock copolymers which are formed with two biocompatible polyethylene blocks. Due to the hydrophobicity of the naphthalocyanines, excess surfactant can be removed at low temperatures through membranes while the dye is fully retained in the micelles. Here, we have noninvasively delineated two separate lymphatic systems and SLNs in

small animals *in vivo* with combination of dual-color nanonaps and PAI. Further, the deep imaging penetration (~ 10 mm) in biological tissues was also achieved with aid of highly absorbing nanonaps *in vivo*. Therefore, we expect nanonaps to be beneficial in breast cancer staging as minimally invasive or noninvasive PA lymph node tracers.

2. Materials and Methods

2.1 Nanonap formation: 2 mg 5,9,14,18,23,27,32,36-octabutoxy, 2,3-naphthalocyanine (ONc) or 2,11,20,29,tetra-tert-butyl-2,3-naphthalocyanine (ZnBNc) was dissolved in 1 ml dichloromethane solvent, then the organic solution was added drop wise to 10 ml 10% (w/v) Pluronic F127 solution and was stirred until the dichloromethane evaporated. After centrifugation at 3,500 g for 10 min, the supernatant were subjected to centrifugal filtration using Amicon Ultra-15 centrifugal filtration device with a 100,000 MWCO (Fisher #UFC9-100-24) at 4 °C until 200 µL of solution was retained in the filtration device. Water was then added back to the filtration device and the washing procedure was repeated in triplicate. Absorbance was measured with a Lambda 35 UV/VIS spectrophotometer (Perkin Elmer).

2.2 Photoacoustic imaging system: A dark-field PAI system (Fig. S1) was utilized in all imaging studies [28]. We used a tunable OPO laser (Surelite OPO PLUS; Continuum) pumped by a Q-switch Nd:YAG laser (Surelite III-10; Continuum) to generate laser pulses with a pulse width of 4 ns and a repetition rate of 10 Hz. Optical wavelengths of 707 and 860 nm which match the optical absorption peaks of nanonaps were selected for *in vivo* and *ex vivo* PA imaging. After going through a spherical conical lens and hand-made optical condenser, the donut-shaped laser beam illuminated into targets. The measured laser pulse energy was approximately 1

mJ/cm^2, which satisfies with the safety limit of the American National Standards Institute (ANSI). To enhance acoustic coupling, we used a water bath having a bottom opening covered with a thin membrane. The generated PA signals were detected by a single-element spherically focused ultrasound transducer (V308; Olympus NDT) with a 5-MHz-center-frequency. The lateral and axial resolutions are 590 and 150 μm, respectively. With one laser pulse excitation at a fixed position, 1D depth-resolved PA images along the z axis were acquired, referred to as A-lines. By performing raster scanning along the x axis, 2D depth-sensitive PA images along the x and z axes were obtained. Additional raster scanning along the y axis allowed us to acquire the volumetric PA images. The amplified PA signals were recorded by an oscilloscope (MSO5204; Tektronix).

2.3 *In vitro* analyses of the PA sensitivity and spectrum: To measure the PA sensitivity and spectra of 707 (ZnBNc) and 860 (ONc) nm nanonaps, we prepared ten silicone tubes (508-001, Silastic laboratory tubing) filled with aqueous solutions of water and nanonaps with various concentrations. The silicone tubes were initially fixed onto an acrylic holder having a middle opening, and both distal ends of the tubes were glued using silicone sealant (RTV118, Momentive). Then, the silicon tubes were immersed in the water bath. To acquire the PA spectra, the excitation laser wavelength was tuned from 680 nm to 950 nm. Furthermore, the optical wavelengths of 707 nm and 860 nm were used to measure the PA sensitivities of two types of nanonaps.

2.4 *In vivo* and *ex vivo* PA imaging: We satisfied with the guidelines of Pohang University of Science and Technology (POSTECH) on the care and use of laboratory animals in all animal experiments. First, female Sprague Dawley rats (~250 g) were prepared for *in vivo* single-color PA lymph nodes mapping. A mixed solution of ketamine (85 mg/kg) and xylazine (15 mg/kg)

was used to anesthetize the rats, and then a vaporized-isoflurane system was used to maintain the anesthesia during the *in vivo* experiments. Before PA imaging, the hair in the axillary regions was removed using depilatory gel. The PA images of the axially region were visualized before and after injection of each nanonaps (0.1 mL and 17.1 mg/mL) via the left forepaw pad. We have maintained the temperature of the rats using an electric heating pad. For *in vivo* dual-color lymph nodes mapping, female Balb/c hairless mice (~ 20 g) were prepared. After anesthetizing them, they were positioned on the sample stage, and then the dorsal regions were photoacoustically imaged. After acquiring the control PA image, 707 nm and 860 nm nanonaps (0.01 mL and 17.1 mg/mL) were injected simultaneously throughout the forepaw pads of both sides (i.e., left side; 707 nm nanonap and right side; 860 nm nanonap). After finishing all *in vivo* animal experiments, they were sacrificed using overdosed CO_2 gas, and the lymph nodes were extracted for *ex vivo* PA imaging.

3. Results

Nanonaps were generated as previously described [27]. A dichloromethane solution of naphthalocyanines (Nc) was added to an aqueous surfactant solution of Pluronic F127 and the organic solvent was evaporated, leading to the formation of nanonap frozen micelles. At 4 ℃, free F127 micelles, but not nanonaps, were dissociated into small F127 unimers, allowing for removal of the free surfactant with low temperature centrifugal filtration. The frozen micelles were induced by the highly hydrophobic Nc dyes used, as shown in Fig. 1A. The 707 nm nanonaps were formed using 2,11,20,29,tetra-tert-butyl-2,3-naphthalocyanine and the 860 nm nanonaps were formed using 5,9,14,18,23,27,32,36-octabutoxy,2,3-naphthalocyanine. Nanonaps were stable in serum, a typical biological fluid, for extended incubation time (Fig. S2). As shown

7

in Fig 1B, these wavelengths represent the peak absorption wavelength of the purified nanoparticulate aqueous solution. The absorption peaks were sufficiently resolved to distinguish the two nanonaps unambiguously without immediately requiring spectral unmixing algorithms. As shown in Fig. 1C, the size of both types of nanonaps was approximately 20 nm. The PA sensitivities of 707 nm and 860 nm nanonaps were estimated by measuring the PA amplitudes at various concentrations (Fig. 1D, 707 nm nanonaps and Fig. 1E, 860 nm nanonaps). As the concentrations of the nanonaps increase, the PA amplitudes linearly increase with R^2 values of 98 and 97 % for 707 and 860 nm nanonaps, respectively. The minimum detectable concentration of 707 and 860 nm nanonaps were both 133.6 μg/mL with signal-to-noise ratios (SNRs) of 2.04 dB and 2.60 dB, respectively. The noise equivalent sensitivities of 707 nm and 860 nm nanonaps are 65.5 μg/mL and 51.4 μg/mL, respectively. The PA spectral properties of the 707 nm and 860 nm nanonaps at concentrations of 4.3 mg/mL were examined (Fig. 1F). Each PA spectral profile is generally similar to the optical absorption spectrum of each nanonap.

To investigate *in vivo* noninvasive PA SLN identification, we independently injected 707 and 860 nm nanonaps into rats' forepaws with a concentration of 17.1 mg/mL and a dose of 100 μL. Figs. 2A and H show the photographs of the hair-removed rats acquired before *in vivo* PA imaging. The black dotted boxes in Figs. 2A and H represent the scanned areas. Before the independent injection of each nanonap, we acquired control PA images (Figs. 2B and I), respectively. The control PA maximum amplitude projection (MAP) images clearly visualized axillary vasculatures with a PA image contrast (i.e., $(PA_{axillary\ vasculatures} - PA_{background})/PA_{background}$) of 8.5 ± 0.7 and 6.4 ± 0.5, but the SLNs were not visible due to their optical transparency. The draining SLN and lymphatic vessels were photoacoustically identified at 28-mins-post-injection (Fig. 2C; 707 nm nanonap and Fig. 2J; 860 nm nanonap). The PA image contrasts of SLNs (i.e.,

8

$(PA_{SLN} - PA_{background})/PA_{background})$ are 32.5 ± 2.8 and 34.4 ± 1.7 in Figs. 2C and 2J, respectively. The PA image contrasts of lymphatic vessels (i.e., $(PA_{lymphatic\ vessels} - PA_{background})/PA_{background})$ are 13.3 ± 3.4 and 25.4 ± 4.6 in Figs. 2C and 2J, respectively. The contrasts of the SLNs with respect to the blood vessels (i.e., $(PA_{SLN} - PA_{blood\ vessels})/PA_{blood\ vessels})$ are 5.2 ± 0.5 and 7.1 ± 0.4 in Figs. 2C and 2J, respectively. The contrasts of the lymphatic vessels with respect to the blood vessels (i.e., $(PA_{lymphatic\ vessels} - PA_{blood\ vessels})/PA_{blood\ vessels})$ are 1.6 ± 0.6 and 5.0 ± 1.1 in Figs. 2C and 2J, respectively. Figs. 2D and 2K show the depth-encoded PA images of Figs. 2C and 2J using pseudo-colors, respectively. The SLNs are located approximately 2.0 – 2.5 mm from the skin surfaces. Figs. 2E and 2L are the depth-resolved PA B-scan images cut along the yellow dotted lines in Figs. 2C and 2J, respectively. Figs. 2E and 2L show clearly the SLNs filled with 707 nm and 860 nm nanonaps, respectively. Then, we layered chicken breast tissues on top of the rats to increase the imaging depth from 2 mm to 6 mm (Figs. 2F and 2M) and 10 mm (Figs. 2G and 2N) [29, 30]. Regardless the types of nanonaps, the SLNs are clearly delineated at both depths. The PA image contrasts of the SLNs at 6 mm are 6.1 ± 1.0 and 5.0 ± 0.6 in Figs. 2F and 2M, respectively. The PA image contrasts of the SLNs at 10 mm are 2.4 ± 0.4 and 1.9 ± 0.4 in Figs. 2G and 2N, respectively.

After *in vivo* PA imaging, we sacrificed rats and extracted lymph nodes for *ex vivo* PA validation. We also sacrificed a control rat without any injection, and excised lymph nodes. Three axillary lymph nodes including the SLN were removed from each rat. Fig. 3A shows the excised lymph nodes. Then, we photoacoustically investigated the spectral responses of the extracted lymph nodes *ex vivo*. Figs. 3B-I shows the PA images of the excised lymph nodes acquired at 680, 700, 750, 800, 850, 860, 900, and 950 nm, respectively. The spectroscopic PA signals of three SLNs were quantified and normalized in Fig. 3J. The spectral PA responses

measured from the removed SLNs well matched with the *in vitro* optical absorbance (Fig. 1B) and PA (Fig. 1F) measurements of 707 and 860 nm nanonaps. At 707 nm, the PA signal enhancement within the SLN with an injection of 707 nm nanonaps (i.e., ($PA_{SLN\ filled\ with\ nanonap}$/ $PA_{normal\ SLN} - 1) \times 100$) reached 1276 ± 147 %, which was approximately 4 times higher than that of the SLN with an injection of 860 nm nanonaps (312 ± 67 %). On the other hand, at 860 nm, the PA signal enhancement within the SLN with an injection of 860 nm nanonaps reached 870 ± 228 %, which was approximately 2 times higher that of the SLN with an injection of 707 nm nanonaps (433 ± 52 %).

For dual-color PA SLN mapping, we simultaneously injected both 707 and 860 nm nanonaps to left and right forepaws of a BABL/c hairless mouse, respectively. The animal was positioned in the animal holder to image the dorsal plane as shown in Fig. 4F. Before injection, the control PA MAP images were obtained at both 707 and 860 nm as shown in Figs. 4A and B, respectively. In the control PA images, axillary vasculatures are clearly visible with PA image contrasts of 3.2 ± 0.2 (707 nm and Fig. 4A) and 3.5 ± 0.3 (860 nm and Fig. 4B). Figs. 4A-a and b shows the depth-sensitive PA cross-sectional images acquired along the yellow dotted lines a and b in Fig. 4A, and Figs. 4B-a and b shows the PA cross-sectional images obtained along the yellow dotted lines a and b in Fig. 4B. The SNLs and lymphatic vessels are invisible in all control images. After injection, the PA MAP images were acquired at both 707 and 860 nm excitation wavelengths as shown in Figs. 4C and D. With 707 nm laser excitation, lymphatic vessels and a SLN at the left axillary region were clearly delineated (Figs. 4C and 4C-b). The PA image contrasts of the left SLN and left lymphatic vessels are 6.7 ± 0.2 and 11.8 ± 1.5, respectively. The PA contrasts of the left SLN and left lymphatic vessels with respect to the blood vessels are 1.1 ± 0.1 and 2.5 ± 0.4, respectively. One the other hand, with 860 nm laser excitation, lymphatic

vessels and a SLN at the right axillary region are evidently identified (Figs. 4D and 4D-a). The PA image contrasts of the right SLN and right lymphatic vessels are 7.8 ± 0.3 and 6.5 ± 0.4, respectively. The PA contrasts of the right SLN and right lymphatic vessels with respect to the blood vessels are 1.1 ± 0.1 and 0.8 ± 0.1, respectively. Note that weak PA signals were also detected from the right SLN with 707-nm light excitation and the left SLN with 860-nm light excitation. Finally, Fig. 4E shows the overlaid PA MAP image of the lymphatic vessels and SLNs acquired from the left (i.e., 707 nm nanonaps and amber) and right (i.e., 860 nm nanonaps and green) axilla.

After *in vivo* dual-color PA imaging, the mouse was euthanized and both left and right SLNs were removed for *ex vivo* PA validation (Fig. 5A). Then, the spectral PA signals were quantified from the SLNs *ex vivo* at 680, 707, 750, 800, 850, 860, 900 and 950 nm as shown in Figs. 5B-I, respectively. At 707 nm, the PA signal enhancement of the SLN1 excised from the left axillary region (i.e., 707-nm nanonaps injection and 1386 ± 320 %) is 2.6 times stronger than that of the SLN2 did from the right axillary area (i.e., 860-nm nanonaps injection and 533 ± 69 %). The *ex vivo* PA imaging results were opposite at 860 nm (i.e., SLN1, 260 ± 134 % vs. SLN2, 2165 ± 462 %). Figure 5J shows the normalized spectral PA responses of the SLNs, and these *ex vivo* dual-color PA imaging results highly co-related with the *in vitro* optical absorbance (Fig. 1B), *in vitro* spectroscopic PA measurement (Fig. 1F), and *ex vivo* single-color spectral PA measurement (Fig. 3J).

4. Discussion

11

One fundamental advantage of optical techniques such as fluorescence imaging and PA imaging over current clinical modalities such as ultrasound, PET, CT and MR is that optical methods can inherently discriminate multiple optically distinct molecular species simultaneously. While this concept has been demonstrated extensively for multiplexed fluorescence imaging [24, 25], to our knowledge there have been few convincing demonstrations of multispectral contrast lymphatic imaging using PA, despite that PA is better suited for SLN imaging, given its far superior depth capabilities. The lack of exploration for multispectral contrast SLN imaging in PA could be for several reasons: 1) PA instrumentation is still rapidly evolving and multi-spectral lasers and systems are still improving. Once tunable lasers with broader spectral coverage are more available, more PA chromophores will be accessible. 2) Compared to PA agents, fluorophores have distinct excitation and emission properties that enable improved resolution of different species; 3) Most PA-active nanoparticles have broad absorption peaks that inhibit spectral resolution; 4) Many PA-active chromophores either cannot be concentrated to high absorption values for injection, or shift their spectral properties at higher concentrations. Nanonaps directly address the last two issues mentioned. Their absorption values are sufficiently narrow to resolve and solutions of nanonaps routinely have absorption values greater than 1000. Previously, it was shown that nanonaps, but not small molecule NIR dyes, have consistent peak absorbance wavelengths over a range of concentrations [27]. Practically, it should be possible to simultaneously monitor the different drainage patterns and mixing of multiple lymphatic systems *in vivo*. In addition, our method can be a potential tool to interpret two independent features in a single image. Further, multi-color and multi-agent imaging could be significantly beneficial to the more complicated lymphatics such as the lymphatic systems in head and neck.

12

Currently, the maximum penetration depth is approximately 1 cm in biological tissues because the used laser pulse energies were ~ 1 mJ/cm^2, which are much less than the ANSI limit. If we improved the light delivery system, more light can be delivered to enhance the penetration depth. In addition, the imaging depth can be much more improved if a clinical PA imaging system is used [10-13]. Further, the averaged depth of the top surface of the axillary human SLNs is only ~12 ± 5 mm below the skin surface. Additionally, the clinical PA imaging system with an US array system will reduce the scanning time, and eventually real-time PA imaging is possible. Although methylene blue is the clinical used tracer for SLN mapping, the cellular toxicity of nanonaps is superior to that of methylene blue [27]. Further, the molar extinction coefficient of the naphthalocyanine derivative dye in the ONc nanonaps (i.e., 1.5×10^5 M^{-1}cm^{-1}) is approximately 2 times higher than that of methylene blue (i.e., 7.4×10^5 M^{-1}cm^{-1}) [31].

5. Conclusion

To our knowledge, this is the first convincing demonstration of simultaneous dual-color PA imaging of two separate lymphatic systems *in vivo*. Further, dual-color organic nanoformulated naphthalocyanines (nanonaps) have been successfully synthesized and demonstrated as excellent PA SLN tracers *in vivo*. The key features of nanonaps include: (1) exceptional optical absorption in the NIR region, (2) spectral stability at a very high concentration, and (3) no heavy metal toxicity. If combined with a clinical PA imaging system, this approach may potentially provide new methodology for minimally invasive or noninvasive method for axillary node mapping staging in breast cancer patients. Additionally, if *in vivo* dual-color PA imaging is integrated with

13

bioconjugated nanonaps, this method can be applied to identify migration and metastasis of cancer cells within lymphatic systems.

Captions

Fig. 1. Formation of nanonap, and optical and photoacoustic properties. (A) Chemical structure of naphthlocyanines used in this study. 707 nm nanonaps are formed with: M = Zn; R1= t-Bu; R2 = H. 860 nm nanonaps are formed with: M = 2H; R1= H; R2 = O-(CH2)3CH3. (B) Normalized optical absorbance and photograph of 707 nm (left, green) and 860 nm nanonaps (right, amber) in water. (C) Dynamic light scattering of 707 nm nanonaps (green) and 860 nm nanonaps (amber). (D and E) PA signal amplitude per different concentration of 707 nm (green) and 860 nm (amber) nanonaps, respectively. (F) Spectral PA responses of 707 nm (green) and 860 (amber) nm nanonaps.

Fig. 2. *In vivo* noninvasive PA imaging of rat's SLNs with injection of 707 nm and 860 nm nanonaps. (A and H) Photographs of the rats taken before *in vivo* imaging. (B and I) Control PA MAP images at 707 nm and 860 nm, respectively. Only axillary blood vessels are visible. (C and J) PA MAP images obtained at 28–min-post-injection of 707 nm and 860 nm nanonaps, respectively. The SLNs and lymphatic vessels are clearly visualized. (D and K) Depth-encoded PA images of (C and J), respectively. (E and L) Cross-sectional PA B-scan images cut along the yellow dotted lines in (C and J), respectively. (F and M) Cross-sectional PA B-scan images of the SLNs with injection of 707 nm and 860 nm nanonaps, respectively, and the PA images were acquired with one layer of chicken breast tissue atop of the rats. (G and N) Cross-sectional PA B-scan images of the SLNs with injection of 707 nm and 860 nm nanonaps, respectively, and the PA images were acquired with two layers of chicken breast tissue atop the rats. PA, photoacoustic; MAP, maximum amplitude projection; SLN, sentinel lymph node; LV, lymphatic vessel; and BV, blood vessel.

Fig. 3. *Ex vivo* spectroscopic PA imaging of excised lymph nodes. (A) Photograph of removed lymph nodes. L1-3, LNs excised from the axillary region of a normal rat; L4-6, SLN and successive LNs excised from the axillary region of a rat with an injection of 707-nm-nanonaps, respectively; and L7-9, SLN and successive LNs excised from the axillary region of a rat with an injection of 860-nm-nanonaps, respectively. *Ex vivo* PA images of the removed lymph nodes acquired at (B) 680, (C) 707, (D) 750, (E) 800, (F) 850, (G) 860, (H) 900, and (I) 950 nm. (J) Quantification of normalized spectroscopic PA signal enhancements calculated from the SLNs. PA, photoacoustic; SLN, sentinel lymph node; and LNs, lymph nodes.

Fig. 4. *In vivo* simultaneous dual-color PA imaging of a rat's SLNs with injection of dual-color nanonaps (707 and 860 nm). (A) Control PA MAP image at 707 nm. (A-a and A-b) Control PA cross-sectional images of right and left axillary regions cut along the dotted lines a and b in (A), respectively. (B) Control PA MAP image at 860 nm. (B-a and B-b) Control PA cross-sectional images of left and right axillary regions cut along the dotted lines a and b in (B), respectively. 707 nm and 860 nm nanonaps (0.01 mL and 17.1 mg/mL) were injected simultaneously

throughout the forepaw pads of both sides (i.e., left side; 707 nm nanonap and right side; 860 nm nanonap). (C) Post-injection PA image at 707 nm. (C-a and C-b) Corresponding PA cross-sectional PA images cut along the dotted lines a and b in (C). (D) Post-injection PA image at 860 nm. (D-a and D-b) Corresponding PA cross-sectional PA images cut along the dotted lines a and b in (D). (E) Overlaid dual-color PA image of both right and left lymphatic systems. (F) Photograph of the dorsal region of the animal. SLN, sentinel lymph node; LV, lymphatic vessel; H, head; and T, tail.

Fig. 5. *Ex vivo* spectroscopic PA imaging of excised SLNs after *in vivo* dual-color PA mapping. (A) Photograph of extracted SLNs. The SLN1 was excised from the left axillary region with 707-nm nanonaps injection, while the SLN2 was from the right side with 860-nm nanonaps injection. *Ex vivo* PA images of the excised SLNs acquired at (B) 680, (C) 707, (D) 750, (E) 800, (F) 850, (G) 860, (H) 900, and (I) 950 nm. (J) Quantification of normalized spectroscopic PA signal enhancements calculated from the SLNs. PA, photoacoustic and SLN, sentinel lymph node.

Figures

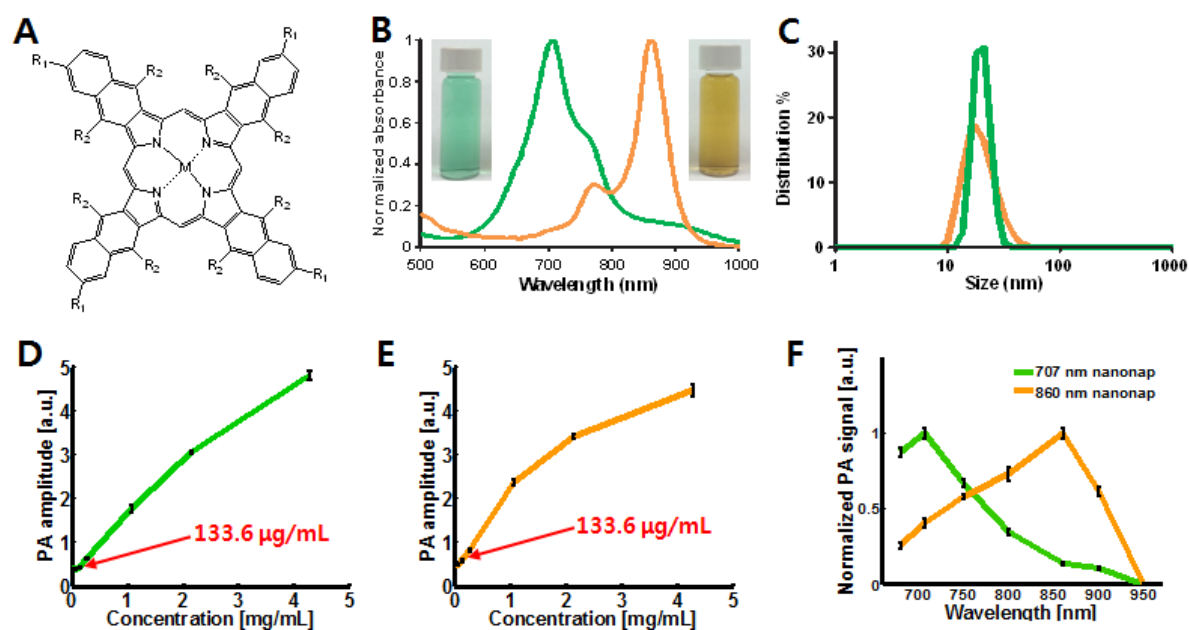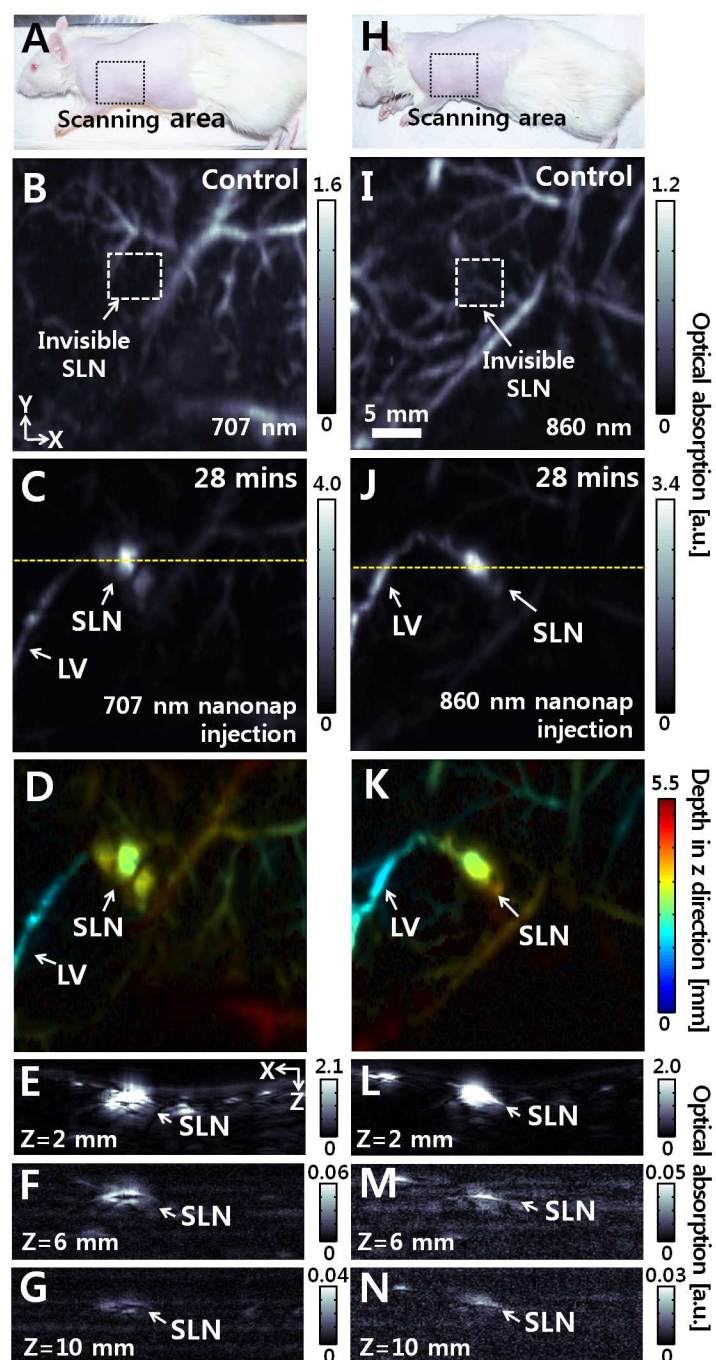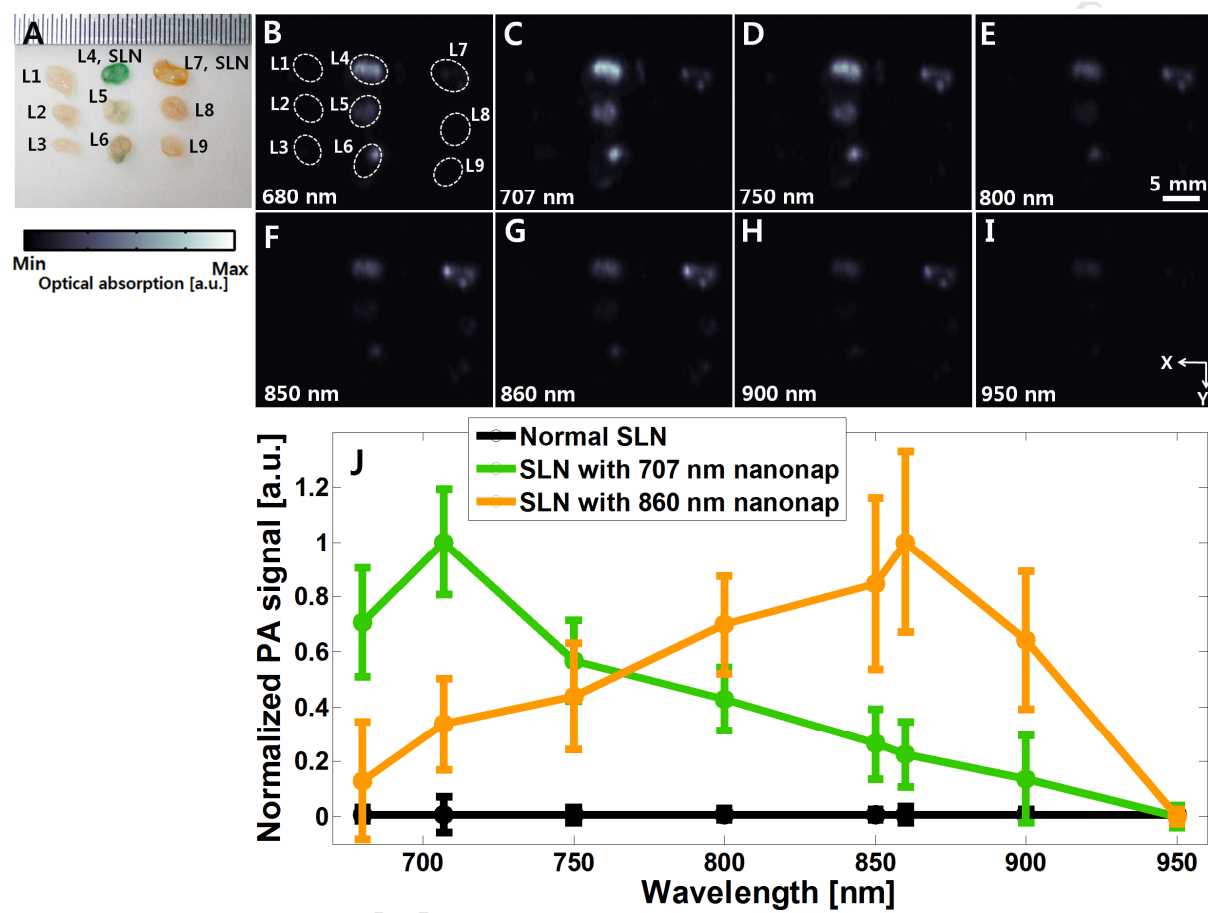**Fig.1**

Fig.2

Fig. 3

Fig.4

Fig.5

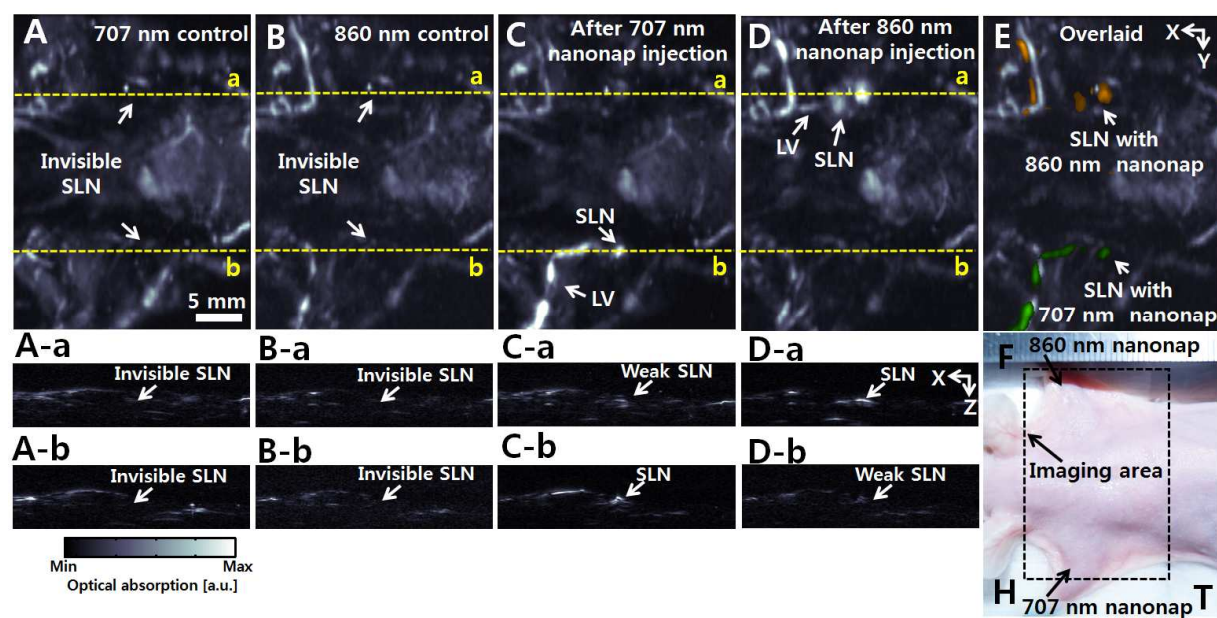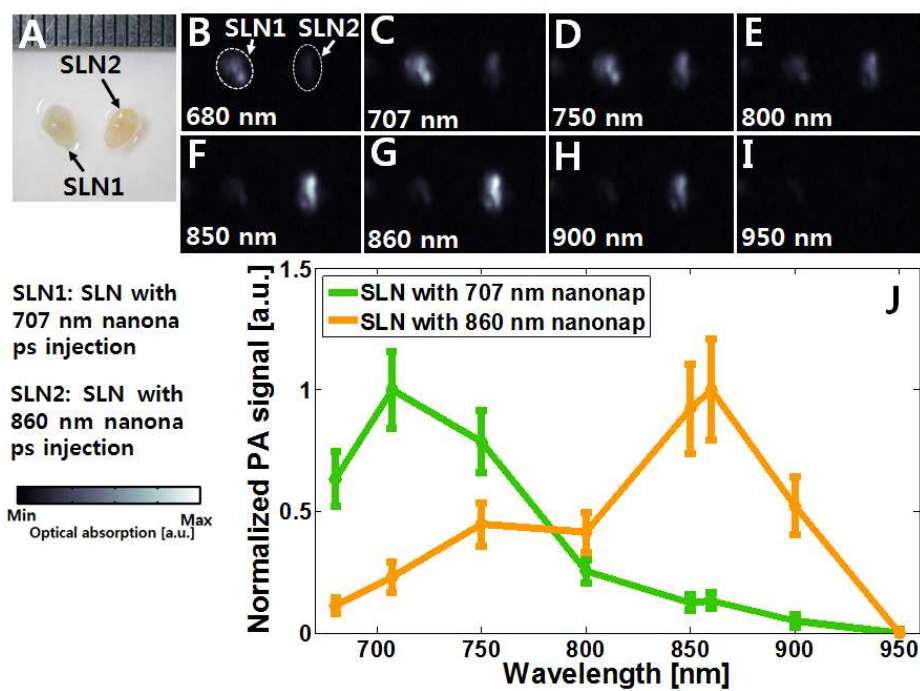**References**

[1] Veronesi U, Paganelli G, Viale G, Galimberti V, Luini A, Zurrida S, et al. Sentinel Lymph Node Biopsy and Axillary Dissection in Breast Cancer: Results in a Large Series. Journal of the National Cancer Institute. 1999;91:368-73.

[2] McMasters KM, Tuttle TM, Carlson DJ, Brown CM, Noyes RD, Glaser RL, et al. Sentinel Lymph Node Biopsy for Breast Cancer: A Suitable Alternative to Routine Axillary Dissection in Multi-Institutional Practice When Optimal Technique Is Used. Journal of Clinical Oncology. 2000;18:2560-6.

[3] Lyman GH, Giuliano AE, Somerfield MR, Benson AB, Bodurka DC, Burstein HJ, et al. American Society of Clinical Oncology Guideline Recommendations for Sentinel Lymph Node Biopsy in Early-Stage Breast Cancer. Journal of Clinical Oncology. 2005;23:7703-20.

[4] Morton DL, Wen D, Wong JH, et al. TEchnical details of intraoperative lymphatic mapping for early stage melanoma. Archives of Surgery. 1992;127:392-9.

[5] Krag DN, Weaver DL, Alex JC, Fairbank JT. Surgical resection and radiolocalization of the sentinel lymph node in breast cancer using a gamma probe. Surgical Oncology. 1993;2:335-40.

[6] Schrenk P, Rieger R, Shamiyeh A, Wayand W. Morbidity following sentinel lymph node biopsy versus axillary lymph node dissection for patients with breast carcinoma. Cancer. 2000;88:608-14.

[7] Purushotham AD, Upponi S, Klevesath MB, Bobrow L, Millar K, Myles JP, et al. Morbidity After Sentinel Lymph Node Biopsy in Primary Breast Cancer: Results From a Randomized Controlled Trial. Journal of Clinical Oncology. 2005;23:4312-21.

[8] Koyama Y, Talanov VS, Bernardo M, Hama Y, Regino CAS, Brechbiel MW, et al. A dendrimer-based nanosized contrast agent dual-labeled for magnetic resonance and optical fluorescence imaging to localize the sentinel lymph node in mice. Journal of Magnetic Resonance Imaging. 2007;25:866-71.

[9] Oyen RH, Van Poppel HP, Ameye FE, Van de Voorde WA, Baert AL, Baert LV. Lymph node staging of localized prostatic carcinoma with CT and CT-guided fine-needle aspiration biopsy: prospective study of 285 patients. Radiology. 1994;190:315-22.

[10] Kim C, Erpelding TN, Jankovic L, Wang LV. Performance benchmarks of an array-based hand-held photoacoustic probe adapted from a clinical ultrasound system for non-invasive sentinel lymph node imaging. Philosophical Transactions of the Royal Society A: Mathematical, Physical and Engineering Sciences. 2011;369:4644-50.

[11] Kim C, Erpelding TN, Jankovic L, Pashley MD, Wang LV. Deeply penetrating in vivo photoacoustic imaging using a clinical ultrasound array system. Biomedical optics express. 2010;1:278-84.

[12] Erpelding TN, Kim C, Pramanik M, Jankovic L, Maslov K, Guo Z, et al. Sentinel Lymph Nodes in the Rat: Noninvasive Photoacoustic and US Imaging with a Clinical US System. Radiology. 2010;256:102-10.

[13] Erpelding TN, Garcia-Uribe A, Krumholz A, Ke H, Maslov K, Appleton C, et al. A dual-modality photoacoustic and ultrasound imaging system for noninvasive sentinel lymph node detection: preliminary clinical results. 2014. p. 894359--6.

[14] Song L, Kim C, Maslov K, Shung KK, Wang LV. High-speed dynamic 3D photoacoustic imaging of sentinel lymph node in a murine model using an ultrasound array. Medical physics. 2009;36:3724-9.

[15] Kim C, Song KH, Gao F, Wang LV. Sentinel Lymph Nodes and Lymphatic Vessels: Noninvasive Dual-Modality in Vivo Mapping by Using Indocyanine Green in Rats—Volumetric Spectroscopic Photoacoustic Imaging and Planar Fluorescence Imaging. Radiology. 2010;255:442-50.

[16] Akers WJ, Edwards WB, Kim C, Xu B, Erpelding TN, Wang LV, et al. Multimodal sentinel lymph node mapping with single-photon emission computed tomography (SPECT)/computed tomography (CT) and photoacoustic tomography. Translational Research. 2012;159:175-81.

[17] Rieffel J, Chen F, Kim J, Chen G, Shao W, Shao S, et al. Hexamodal Imaging with Porphyrin-Phospholipid-Coated Upconversion Nanoparticles. Advanced Materials. 2015;27:1785-90.

[18] Liu X, Lee C, Law W-C, Zhu D, Liu M, Jeon M, et al. Au–Cu2–xSe Heterodimer Nanoparticles with Broad Localized Surface Plasmon Resonance as Contrast Agents for Deep Tissue Imaging. Nano Lett. 2013;13:4333-9.

[19] Liu X, Law W-C, Jeon M, Wang X, Liu M, Kim C, et al. Cu2–xSe Nanocrystals with Localized Surface Plasmon Resonance as Sensitive Contrast Agents for In Vivo Photoacoustic Imaging: Demonstration of Sentinel Lymph Node Mapping. Advanced Healthcare Materials. 2013;2:952-7.

[20] Jasung K, Mansik J, Yunok O, Hyun Wook K, Jeehyun K, Chulhong K, et al. In vivo non-ionizing photoacoustic mapping of sentinel lymph nodes and bladders with ICG-enhanced carbon nanotubes. Physics in medicine and biology. 2012;57:7853.

[21] Geoffrey PL, Ashvin B, Kimberly AH, Suraj M, Yun-Sheng C, Stanislav YE. Silica-coated gold nanoplates as stable photoacoustic contrast agents for sentinel lymph node imaging. Nanotechnology. 2013;24:455101.

[22] de la Zerda A, Bodapati S, Teed R, May SY, Tabakman SM, Liu Z, et al. Family of Enhanced Photoacoustic Imaging Agents for High-Sensitivity and Multiplexing Studies in Living Mice. ACS nano. 2012;6:4694-701.

[23] Troyan S, Kianzad V, Gibbs-Strauss S, Gioux S, Matsui A, Oketokoun R, et al. The FLARE™ Intraoperative Near-Infrared Fluorescence Imaging System: A First-in-Human Clinical Trial in Breast Cancer Sentinel Lymph Node Mapping. Annals of surgical oncology. 2009;16:2943-52.

[24] Kobayashi H, Koyama Y, Barrett T, Hama Y, Regino CAS, Shin IS, et al. Multimodal Nanoprobes for Radionuclide and Five-Color Near-Infrared Optical Lymphatic Imaging. ACS nano. 2007;1:258-64.

[25] Kobayashi H, Hama Y, Koyama Y, Barrett T, Regino CAS, Urano Y, et al. Simultaneous Multicolor Imaging of Five Different Lymphatic Basins Using Quantum Dots. Nano Lett. 2007;7:1711-6.

[26] Kim S, Lim YT, Soltesz EG, De Grand AM, Lee J, Nakayama A, et al. Near-infrared fluorescent type II quantum dots for sentinel lymph node mapping. Nat Biotech. 2004;22:93-7.

[27] Zhang Y, Jeon M, Rich LJ, Hong H, Geng J, Zhang Y, et al. Non-invasive multimodal functional imaging of the intestine with frozen micellar naphthalocyanines. Nat Nano. 2014;9:631-8.

[28] Kim C, Jeon M, Wang LV. Nonionizing photoacoustic cystography in vivo. Optics letters. 2011;36:3599-601.

[29] Marquez G, Wang LV, Lin S-P, Schwartz JA, Thomsen SL. Anisotropy in the absorption and scattering spectra of chicken breasttissue. Appl Opt. 1998;37:798-804.

[30] Tromberg BJ, Coquoz O, Fishkin JB, Pham T, Anderson ER, Butler J, et al. Non–invasive measurements of breast tissue optical properties using frequency–domain photon migration. Philosophical Transactions of the Royal Society of London B: Biological Sciences. 1997;352:661-8.

[31] Kim C, Favazza C, Wang LV. In Vivo Photoacoustic Tomography of Chemicals: High-Resolution Functional and Molecular Optical Imaging at New Depths. Chemical reviews. 2010;110:2756-82.
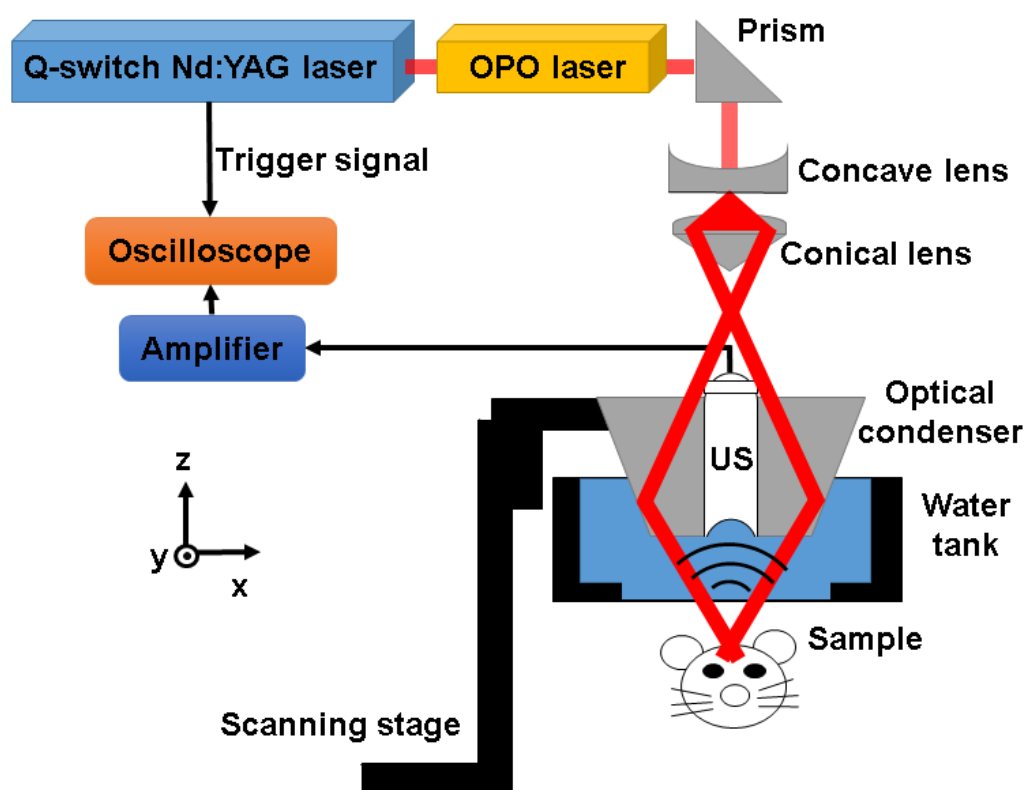
Supporting Information

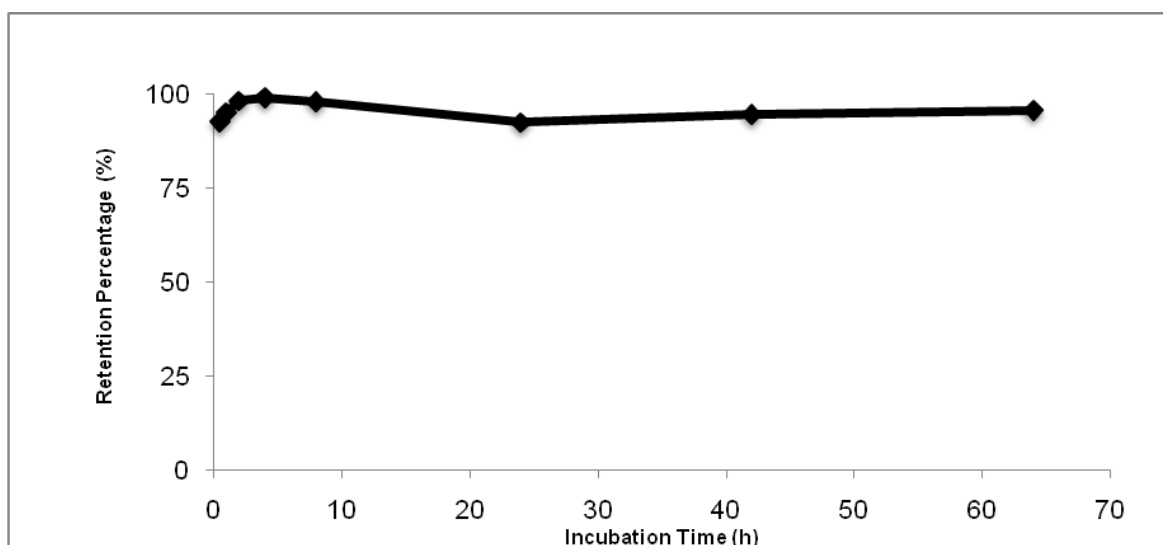**Fig. S1.** Schematic of a photoacoustic imaging system. US, ultrasound transducer.

Fig. S2. Stability of 860 nm nanonaps in serum. Nanonaps were incubated in Serum (serum:ONc solution (v/v)=1:1) and absorbance was checked at the time point shown.